# Comparison study of catalyst nanoparticle formation and carbon nanotube growth: Support effect

Cite as: J. Appl. Phys. **101**, 124310 (2007); https://doi.org/10.1063/1.2749412
Submitted: 26 January 2007 • Accepted: 14 May 2007 • Published Online: 26 June 2007

**Yunyu Wang, Zhiquan Luo, Bin Li, et al.**

# Comparison study of catalyst nanoparticle formation and carbon nanotube growth: Support effect

Yunyu Wang,[a] Zhiquan Luo, Bin Li, and Paul S. Ho
*Microelectronics Research Center, The University of Texas at Austin, Austin, Texas 78712*

Zhen Yao
*Department of Physics, The University of Texas at Austin, Austin, Texas 78712*

Li Shi
*Department of Mechanical Engineering, The University of Texas at Austin, Austin, Texas 78712*

Eugene N. Bryan
*Department of Material Science and Engineering, North Carolina State University, Raleigh, North Carolina 27595*

Robert J. Nemanich
*Department of Physics, Arizona State University, Tempe, Arizona 85287*

(Received 26 January 2007; accepted 14 May 2007; published online 26 June 2007)

A comparison study has been conducted on the formation of catalyst nanoparticles on a high surface tension metal and low surface tension oxide for carbon nanotube (CNT) growth via catalytic chemical vapor deposition (CCVD). Silicon dioxide ($SiO_2$) and tantalum have been deposited as supporting layers before deposition of a thin layer of iron catalyst. Iron nanoparticles were formed after thermal annealing. It was found that densities, size distributions, and morphologies of iron nanoparticles were distinctly different on the two supporting layers. In particular, iron nanoparticles revealed a Volmer-Weber growth mode on $SiO_2$ and a Stranski-Krastanov mode on tantalum. CCVD growth of CNTs was conducted on iron/tantalum and iron/$SiO_2$. CNT growth on $SiO_2$ exhibited a tip growth mode with a slow growth rate of less than 100 nm/min. In contrast, the growth on tantalum followed a base growth mode with a fast growth rate exceeding 1 $\mu$m/min. For comparison, plasma enhanced CVD was also employed for CNT growth on $SiO_2$ and showed a base growth mode with a growth rate greater than 2 $\mu$m/min. The enhanced CNT growth rate on tantalum was attributed to the morphologies of iron nanoparticles in combination with the presence of an iron wetting layer. The CNT growth mode was affected by the adhesion between the catalyst and support as well as CVD process.
 [DOI: 10.1063/1.2749412]

## I. INTRODUCTION

Carbon nanotubes (CNTs) exhibit unusual electrical, thermal, and mechanical properties,[1–3] and they have shown great potential for applications as nanoelectronic devices[4] and interconnects,[5] gas and water filters which can enhance gas and water permeabilities by several orders of magnitude,[6] and CNT polymeric composites for flexible electronic applications.[7]

For various applications, a controlled CNT growth method is indispensable. However, a complete understanding of the growth mechanism of CNTs is still lacking at this time. Briefly, chemical vapor deposition (CVD) growth of CNTs can be described in four stages: (1) adsorption and dissociation of hydrocarbons, (2) carbon diffusion, (3) CNT nucleation, and (4) incorporation of carbon atoms into the tubular structure.[8] In the first stage, adsorption and dissociation of hydrocarbons will vary depending on the specific CVD method used. In catalytic CVD (CCVD), dissociation of hydrocarbons is primarily facilitated by catalysts. In contrast, in plasma CVD, high frequency electromagnetic fields break hydrocarbons into ions, electrons, and free radicals, which in combination with plasma reactive etching by hydrogen, oxygen, or ammonia[9,10] significantly increases the adsorption and dissociation of hydrocarbons. In the second stage, adsorbed carbon atoms diffuse either on the catalyst surface (surface diffusion) or into the bulk of the catalyst (bulk diffusion). It has been found that the contribution of the two diffusion processes depends on the catalyst nanoparticle size.[11] Surface diffusion dominates for small catalyst particles with size less than 20 nm due to the large surface area to volume ratio.[8,12] For larger catalyst particles (>100 nm) bulk diffusion becomes the major mass transport mechanism.[13] For catalyst particles with intermediate sizes, contributions from bulk and surface diffusion processes are comparable.[11,14] In the third stage, carbon atoms start interconnecting with each other on the catalyst surface, and by the confinement of the catalyst nanoparticle shape, the cap of the CNT is formed. In the last stage, carbon atoms are continuously incorporated into the root of the CNT cap, and finally, the cap starts extruding out of the catalyst nanoparticle resulting in CNT growth. The CNT growth rate $G_r$ can

[a]Author to whom correspondence should be addressed; electronic mail: yywang@mail.utexas.edu

 

be described by an Arrhenius equation $G_r = A \exp^{-E_a/KT}$, where $A$ is a constant, and $E_a$ is the activation energy. For the aforementioned four sequential stages, the rate-limiting step corresponds to the slowest process with the largest activation energy barrier.

CNTs have exhibited two growth modes, namely, base and tip growth, and it has been suggested that the observed mode depends on the adhesion between the catalyst and substrate.[13] The base growth mode corresponds to strong adhesion. In this mode catalyst particles bond strongly with the substrate during growth, and nanotube growth occurs on the top of the catalysts.[11,15] In tip growth mode, CNT walls extrude out from the bottom of the catalyst particles. Because of the weak catalyst-substrate adhesion the catalyst particles then arise as the CNTs continue to grow from the substrate, and they finally appear at the tips of CNTs.[16]

Catalysts are critical for CNT growth. Previous studies have explored methods to improve catalyst efficiency for enhancing nanotube yields and growth of CNTs on metal contacts including the use of bimetallic catalysts[17,18] and multimetal layers.[19,20] The use of aluminum (Al) was particularly effective in improving the growth yield of small diameter CNTs. This has been attributed to the effect of aluminum on the segregation of small catalyst particles.[21–23] In addition to the catalytic activity, i.e., adsorption and dissociation of hydrocarbon precursors, the size of catalyst nanoparticles plays a key role in CNT growth. Different catalyst particle sizes can lead to three different carbon nanostructures: hollow nanotubes for small catalyst particles, bamboolike nanofibers for intermediate sizes, and carbon fibers for large catalyst particles.[11]

Since for microelectronic applications CNTs have been grown on either metal or oxide support, it is of great interest to understand the formation of catalyst nanoparticles and CNT growth on these supporting materials. In a recent study,[24] we observed that a Ta supporting layer greatly facilitated the CCVD growth of vertical, dense multiwalled CNTs from Fe nanoparticles deposited on the Ta layer. Here, we further investigate, in detail, the effects of the supporting layer on the morphologies of Fe catalyst nanoparticles and subsequent growth of CNTs by both CCVD and plasma enhanced CVD (PECVD). As reported in our previous work,[24] the supporting layer peculiarly affected the contact angles of iron nanoparticles, and the effect was attributed to different surface tensions of the supporting layers and their interfacial energies with the catalyst particles. In the current work, we observed that the supporting layers had broad effects on size distributions, densities, morphologies, and growth modes of catalyst nanoparticles, which deeply impacted CNT growth. In particular, the effects of the catalyst morphology and the presence of wetting layer on CCVD growth of CNTs were discussed in terms of catalyst dynamics and catalyst activity.

## II. EXPERIMENTS

Two supporting layers were used in this study, namely, (i) 300 nm thermally grown $SiO_2$ film on (100) silicon wafers and (ii) a 50 nm tantalum layer deposited on the $SiO_2$ film using dc sputtering. Thin layers of iron catalyst of 1.5–9 nm thick were deposited on the supporting layers using electron beam evaporation. The thicknesses were monitored by a quartz-crystal oscillator and calibrated by atomic force microscopy (AFM) with an uncertainty of 3 Å. For CCVD growth of CNTs, the substrates were transferred into a 1 in. diameter quartz tube furnace (Linderburger/blue). Hydrogen was introduced into the furnace at a flow rate of 1 l/min, and the temperature was ramped up to 700 °C. The furnace was stabilized at 700 °C for 1 min, and acetylene ($C_2H_2$) was admitted at a flow rate of 100 ml/min to initiate nanotube growth. The growth was carried out at ambient pressure and lasted for 5 min. PECVD growth of CNTs was conducted in a 6 in. stainless steel vacuum chamber with a base pressure $<1\times10^{-3}$ Torr. 2.45 GHz microwave generation source was employed to initiate the plasma. Precursor gases used for CNT growth were ammonia ($NH_3$) and acetylene ($C_2H_2$) with a flow rate ratio of 3:1. The growth pressure was 20 Torr, and the growth temperature was ~850 °C. The growth time was 5 min. Detailed growth conditions can be found elsewhere.[25]

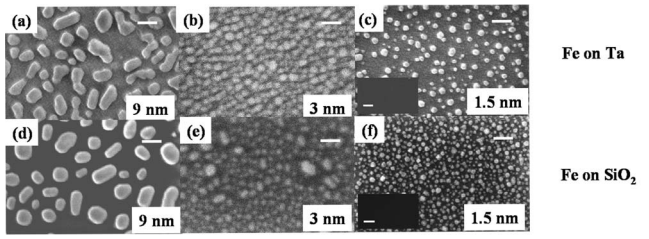


FIG. 1. (Color online) SEM images of morphologies of Fe nanoparticles on Ta with Fe thicknesses of (a) 9 nm, (b) 3 nm, and (c) 1.5 nm; Fe nanoparticles on $SiO_2$ with Fe thicknesses of (d) 9 nm, (e) 3 nm, and (f) 1.5 nm. Inset of (c) and (f) are SEM images of 1.5 nm Fe films on Ta and $SiO_2$ prior to annealing, respectively. Scale bars are (a) 100 nm, (b) 40 nm, (c) 100 nm, (d) 100 nm, (e) 40 nm, and (f) 40 nm, insets in (c) and (f) 200 nm.

To characterize the catalyst nanoparticles, cross-sectional transmission electron microscopy (TEM) (FEI TECNAI G2 F20 X-TWIN TEM) was used. The preparation of TEM samples followed standard procedures of dicing and cutting by focused ion beam (FIB) microprobe. Scanning electron microscopy (SEM) (LEO 1530) was used to observe the morphologies of CNT films and catalyst nanoparticles.

## III. RESULTS

### A. Catalyst nanoparticles

To investigate the formation of Fe nanoparticles on the supporting layers, Fe thin films with different thicknesses, ranging from 1.5 to 9 nm, were annealed at 700 °C for 1 min under hydrogen flow. Prior to annealing, Fe deposited on both Ta and $SiO_2$ appeared as a continuous film with all thicknesses deposited. SEM images of 1.5 nm Fe on Ta and $SiO_2$ prior to annealing are shown in the inset of Figs. 1(c) and 1(f), respectively. After annealing iron nanoparticles were formed on Ta and $SiO_2$, as shown in the SEM images in Figs. 1(a)–1(f). To obtain the size distribution and density of nanoparticles, the images were analyzed by IMAGE-PRO PLUS. The individual nanoparticles were mapped and their sizes were measured. It was found that the nanoparticle size and density varied with the supporting material used and the

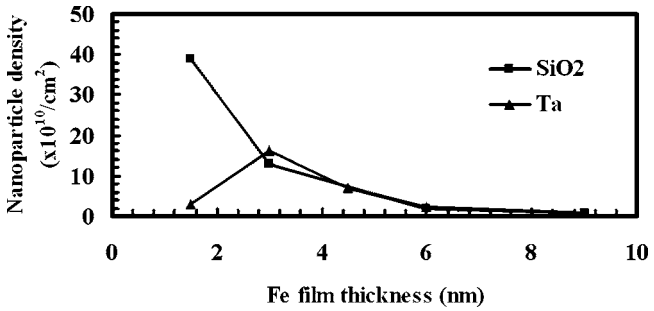


FIG. 2. (Color online) A plot of the correlation between the nanoparticle density and Fe film thickness. Squares denote $SiO_2$ and triangles denote Ta.

thickness of the Fe film. As shown in Fig. 2, on the Ta supporting layer the density of Fe particles shows a peak at 3 nm with a density about $1.6\times10^{11}/cm^2$. In particular, for maximum density at 3 nm, the nanoparticle size distribution is 13–30 nm. In comparison, Fe nanoparticles on $SiO_2$ show a continuous trend of decreasing size and increasing density for Fe thicknesses from 9 to 1.5 nm. For 1.5 nm Fe on $SiO_2$, the Fe particles are distributed narrowly from 4 to 20 nm with a density estimated to be as high as $3.9\times10^{11}/cm^2$. In previous studies, even smaller Fe nanoparticles with higher density were achieved by annealing subnanometer Fe thin films on $SiO_2$.[9,21,26]

High resolution TEM (HRTEM) has been used to examine the cross-sectional morphology, crystalline structure, and chemical profiling of the Fe nanoparticles on $SiO_2$ and Ta, respectively. The examinations have been consistently conducted on samples with the Fe thicknesses of 3 and 9 nm on both supports, and the results are similar. Figure 3(a) exhibits high magnification TEM images of nanoparticles with the Fe thickness of 9 nm on both supports, revealing that the Fe nanoparticles possess crystalline structures on both supporting layers. However, the curvatures of the nanoparticles are distinctly different. On Ta the particles show a hemisphere shape with contact angles less than 90°, while on $SiO_2$ the particles extrude from the substrate with contact angles exceeding 120°. The contact angle distributions of 50 nanoparticles on each support are shown in Fig. 3(b).

Chemical profiling was investigated in scanning transmission electron microscopy (STEM). Figure 4(a) shows STEM images of Fe nanoparticles on two supports with the Fe thickness of 3 nm. *Z* contrast was exhibited in STEM images, i.e., on Ta support Fe appears to be dark and Ta is bright, while on $SiO_2$ support Fe is bright and $SiO_2$ is dark (insets are the low resolution STEM images). By *Z* contrast it appears that an iron wetting layer (WL) is formed on Ta but not on $SiO_2$. To confirm the existence of the iron WL, line-scan electron energy loss spectroscopy (EELS) was carried out, and the scanning lines were selected especially across the regions between the nanoparticles [as shown in Fig. 4(a)]. The scan started from the red dot (the origin point), went down along the scanning line, and ended in the supporting layer, as shown in Fig. 4(a). A series of depth-dependent spectra along the scanning line for Fe/Ta and $Fe/SiO_2$ was shown in Fig. 4(b), respectively. It was found that there was no evidence of Fe on $SiO_2$ between the Fe nanoparticles. However, Fe was found on the Ta surface between nanoparticles confirming the existence of the iron WL.

### B. CNTs grown by CCVD

As-grown CNTs show distinctly different morphologies on Fe/Ta and $Fe/SiO_2$. On the Ta supporting layer, vertically

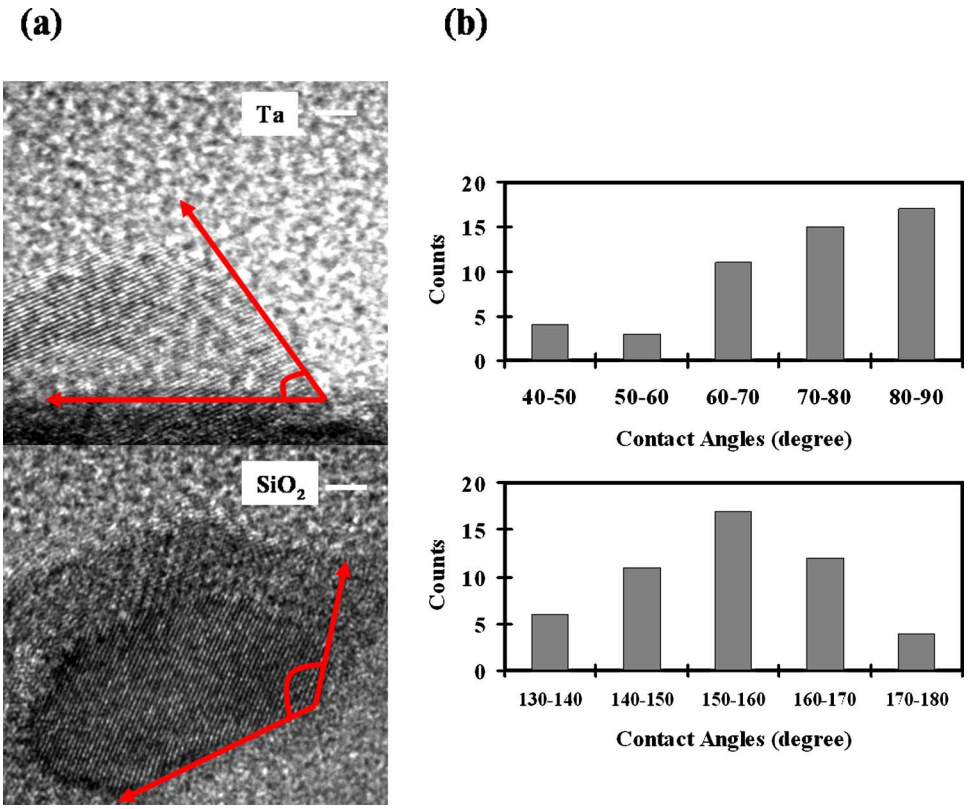


FIG. 3. (Color online) (a) High resolution cross-sectional TEM images of Fe nanoparticle on Ta and $SiO_2$ with the Fe thickness of 9 nm. Fe particles on Ta show a hemisphere shape with relatively small contact angles of $\leqslant 90°$, while Fe particles on $SiO_2$ beads up with a large contact angles of $>120°$. (b) Plots of contact angle distribution of Fe nanoparticles on $SiO_2$ and Ta, respectively (for each support, 50 Fe particles were sampled). Scale bars are 2 nm for both Ta and $SiO_2$.

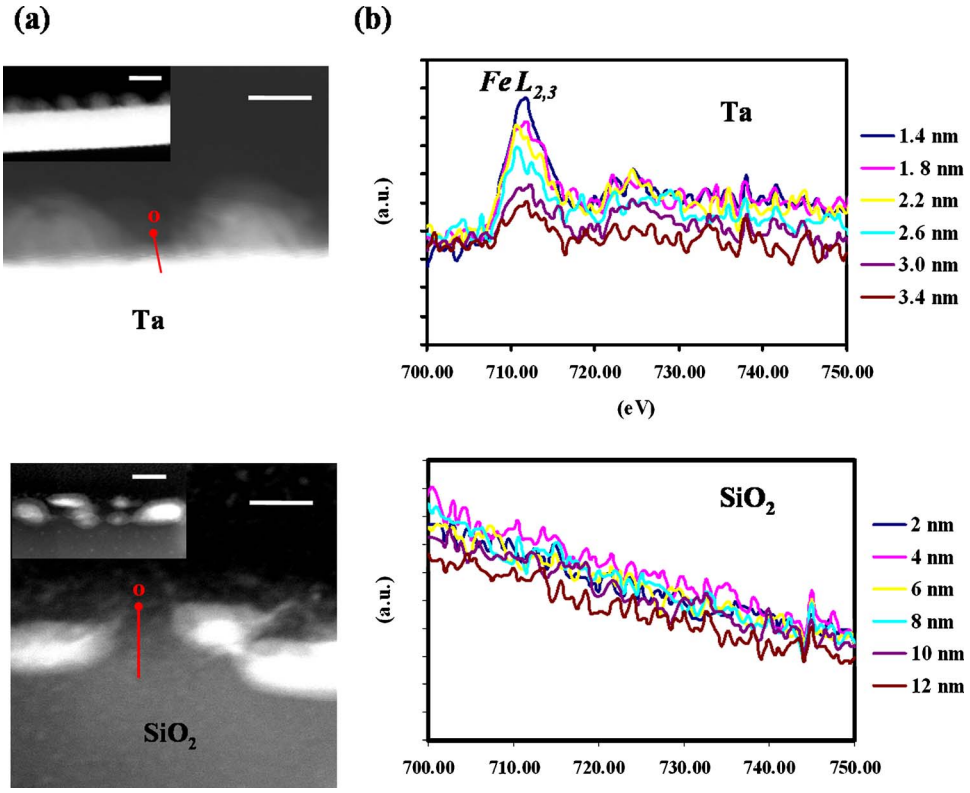


FIG. 4. (Color online) (a) Cross-sectional STEM images of Fe nanoparticles with the Fe thickness of 3 nm on Ta and $SiO_2$ (insets are the low resolution STEM images). *Z* contrast is exhibited in the images, i.e., on Ta support Fe appears to be dark and Ta is bright; whereas on $SiO_2$ support Fe is bright and $SiO_2$ is dark. The red lines are specified for line-scan EELS analysis. The scan starts from the red dot (the origin point) down to inside of the supporting layer. (b) Selected EELS spectra along the red lines in (a), showing that an Fe wetting layer is formed on Ta. Scale bars are 20 nm for Fe/Ta, 10 nm for $Fe/SiO_2$, and 10 nm for both insets.

aligned CNT thin films were obtained for Fe thicknesses from 1.5 to 9 nm, as shown in Figs. 5(a)–5(c). The thickness of CNT films was in the range of 5–10 $\mu$m, with growth rates exceeding 1 $\mu$m/min. Here, the growth rate is estimated by the value of the CNT film thickness/growth time. The density of CNTs was found to depend on the Fe thickness deposited. In particular, vertically aligned, uniform, and dense CNTs were obtained on a 3 nm thick Fe layer, although CNTs on both 9 and 1.5 nm Fe layers exhibited relatively poor vertical alignment. Since alignment of CNTs in CCVD has been attributed to van der Waals forces between crowding nanotubes,[27] poor alignment suggests relatively low densities of CNTs for 9 and 1.5 nm Fe layers compared to those on the 3 nm layer. On $Fe/SiO_2$ supporting layers, very low yields of CNTs were obtained, as exhibited in Figs. 5(d)–5(f). The tubes were randomly distributed on the substrates with average lengths about 100–500 nm. There were some long nanotubes with lengths up to 1–2 $\mu$m but most CNTs obtained were less than 500 nm. The CNT growth rate on $Fe/SiO_2$ was estimated to be less than 100 nm/min. Note that since CNT growth on $Fe/SiO_2$ was not as an aligned film, the growth rate was estimated using the value of the average CNT length/growth time.

TEM images of CCVD grown CNTs on 3 nm Fe/Ta and 3 nm $Fe/SiO_2$ are shown in Fig. 6, where arrows indicate the tips of the CNTs. Figure 6(a) shows CNTs grown on Fe/Ta. The nanotubes appear to be hollow with diameters of 5–10 nm. The tips of CNTs are capped with graphite layers without encapsulated Fe nanoparticles as shown in Fig. 6(b), which suggests a base growth mode. In Fig. 6(c) CNTs grown on $SiO_2$ using CCVD appear to be curly with a tube diameter of about 10 nm. Figure 6(d) shows a tip of a CNT on $SiO_2$ with an encapsulated Fe nanoparticle, where curved graphite layers cover almost all surface areas of the nanoparticle, and nanotube walls extrude out from the bottom of the nanoparticle, indicating a tip growth mode.

### C. CNTs grown by PECVD

Besides using different supporting materials we have also grown CNTs on $Fe/SiO_2$ layers with 1.5–9 nm thick Fe

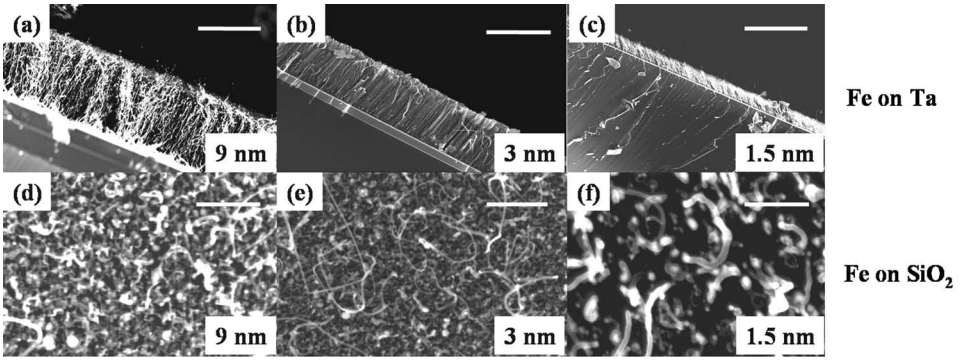


FIG. 5. SEM images of CCVD grown CNT on Ta with Fe thicknesses of (a) 9 nm, (b) 3 nm, and (c) 1.5 nm; CNTs grown on $SiO_2$ with Fe thicknesses of (d) 9 nm, (e) 3 nm, and (f) 1.5 nm. Scale bars are (a) 8 $\mu$m, (b) 8 $\mu$m, (c) 24 $\mu$m, (d) 200 nm, (e) 400 nm, and (f) 200 nm. Note that (a)–(c) are cross-sectional view and (d)–(f) are top view.

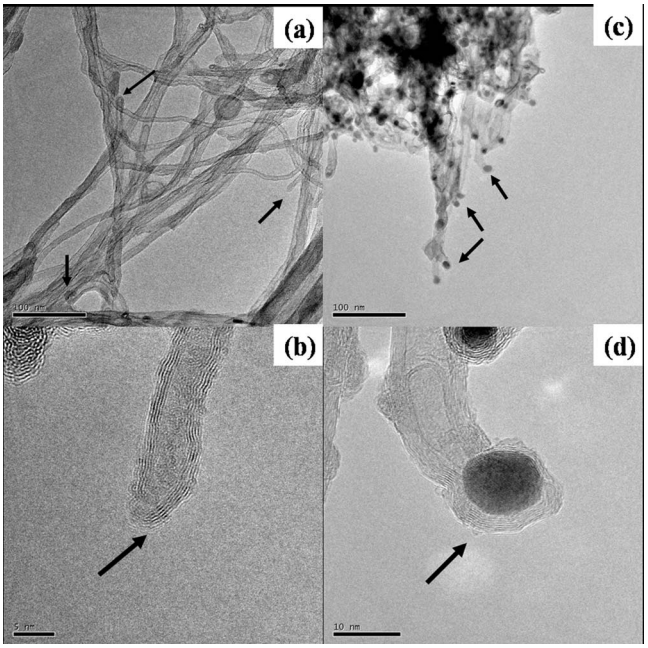


FIG. 6. TEM images of CNTs grown using different supports and CVD processes. (a) and (b) show CNTs grown on Ta by CCVD; (c) and (d) show CNTs grown on $SiO_2$ by CCVD. Arrows in the figures indicate the tips of CNTs. Scale bars are (a) 100 nm, (b) 5 nm, (c) 100 nm, and (d) 10 nm.

using PECVD.[11] A SEM image of vertically aligned CNT films on 3 nm $Fe/SiO_2$ is shown in Fig. 7(a). Compared to the short curly tubes grown by CCVD on $SiO_2$, the CNTs grown by PECVD exhibited a fast growth rate, which was estimated to exceed 2 $\mu$m/min for a film thickness greater than 10 $\mu$m. HRTEM images of CNTs grown by PECVD are shown in Fig. 7(b). The CNTs have diameters of about 25 nm. The arrow shows an enclosed tip without Fe particle indicating a base growth mode. A TEM image of the CNT bottom is also shown in the inset of Fig. 7(b), where a bamboolike internal structure is clearly observed. It should be noted that the growth temperature in PECVD was raised to 850 °C through the combination of sample stage heater and additional heating resulting from the plasma. To investigate whether a high temperature in CCVD enhances nanotube growth on $SiO_2$, we have also grown CNTs on $SiO_2$ at 850 °C in CCVD. However, the yield and morphology of CNTs appear similar as those grown at 700 °C.

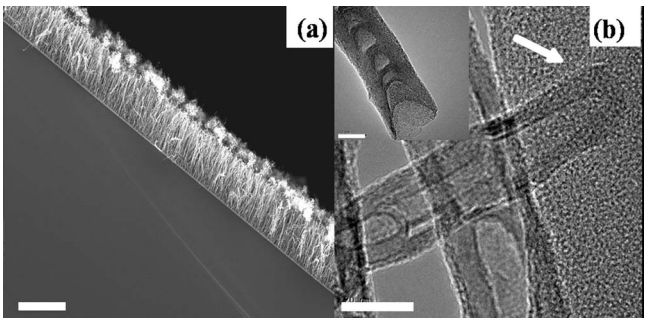


FIG. 7. (a) A cross-sectional SEM image of vertically aligned CNTs grown by PECVD on $SiO_2$. The Fe thickness is 3 nm. (b) A TEM image of a CNT tip grown on $SiO_2$ by PECVD. The arrow denotes the tip of the CNT. Inset of (b) presents a CNT bottom grown on $SiO_2$ by PECVD. Scale bars are (a) 10 $\mu$m, (b) 20 nm, and inset of (b) 20 nm.

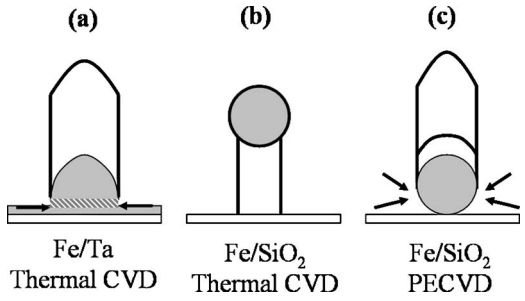


FIG. 8. A schematic of CNT growth modes varying with support materials and CVD processes. (a) The base growth mode for Fe/Ta using CCVD. The strip area on Fe nanoparticle surface denotes uncovered catalyst area, which may help sustain the CNT growth. (b) The tip growth mode for $Fe/SiO_2$ using CCVD. (c) The base growth mode (with bamboolike structure) for $Fe/SiO_2$ using PECVD. Black arrows denote carbon supplies for CNT growth.

As illustrated in Fig. 8, different growth modes were observed depending on the supporting layer materials and CVD process. CNTs grown on Fe/Ta by CCVD and on $Fe/SiO_2$ by PECVD were by the base growth mode, while CNTs grown on $Fe/SiO_2$ by CCVD were by the tip growth mode.

## IV. DISCUSSION

### A. Catalyst nanoparticle

Catalyst nanoparticles with sizes from a few nanometers to several tens of nanometers are critical for CNT growth. To form such nanoparticles, thin catalyst films with a thickness less than 10 nm are usually annealed, a process similar to the formation of self-assembling quantum dots (SAQDs) from strained heteroepitaxial film.[28,29] Considering annealing conditions with a high substrate temperature and no deposition flux, the thin film growth most probably occurs near thermal equilibrium with the film morphologies controlled by thermodynamics rather than kinetics. Accordingly, the morphology of the thin film is governed by minimization of the total free energy $\Delta G$,

$$\Delta G = a\Delta G_v + \sum_i b_i \gamma_i + \Delta U_s, \tag{1}$$

where $a$ and $b_i$ are geometrical constants, $\Delta G_v$ is the free energy change per unit volume, $\gamma_i$ are surface tensions of the supporting layer, the catalyst layer, and interface, respectively, and $\Delta U_s$ is the change of strain energy. Here the strain $\varepsilon$ originates from the lattice mismatch between the film and substrate, i.e., $\varepsilon = |a_0(f) - a_0(s)|/a_0(f)$, with $a_0(f)$ and $a_0(s)$ being lattice constants for the film and substrate, respectively. Three components on the right side of Eq. (1) represent the contributions from the catalyst material itself, the supporting material, and the interactions between each other, and this equation is only valid for describing nanoparticles during annealing. Once CNT growth is involved, the contribution from CNT-catalyst interaction has to be added into Eq. (1).

Based on Eq. (1), the growth of a wetting film, island formation, or ripening can occur and the size and density of the islands can be predicted, depending on the amount of

coverage, the relative strength of the surface tension, and lattice strain.[28] Three film growth modes are commonly observed according to the $\varepsilon$ and surface tension ratio $\kappa = \gamma_s - \gamma_f / \gamma_s$, where subscripts $s$ and $f$ represent the substrate and film, respectively. The Volmer-Weber (VW) mode [three-dimensional (3D) islands] predominates when $\kappa < 0$, which can expand with additional lattice mismatch. In contrast, the Frank–Van der Merwe (FM) mode [two-dimensional (2D) layer by layer] occurs only if $\kappa > 0$ and $\varepsilon$ being very small, and in between the VW and FM modes, Stranski-Krastanov (SK) mode (2D layer-plus-3D island) rules.[30,31]

In our experiments the density and size of Fe nanoparticles vary with the supporting material and initial Fe film thickness. Prior to annealing, Fe deposited on both Ta and $SiO_2$ appeared as a thin film for Fe thicknesses from 15 to 9 nm. After annealing, the maximum density of Fe particles was found at a 3 nm thickness on Ta. Below or above 3 nm, the particle density decreased. However, on $SiO_2$ the nanoparticle density continued to increase as the film thickness was reduced from 9 to 1.5 nm.

Considering the high surface tension of Fe of 1880–2150 ergs/cm$^2$ (Ref. 32) as compared to 43–106 ergs/cm$^2$ for $SiO_2$,[33] the formation of nanoparticles on $SiO_2$ is expected to follow the VW growth mode. The growth starts with the formation of small nuclei, where the islands start to grow with further deposition until the island density reaches saturation. The larger islands form through ripening and coalescence, and consequently the island density decreases. In contrast, Ta has a high surface tension (2100–2200 ergs/cm$^2$),[31] and the surface tension ratio $\kappa$ for Fe/Ta is $>0.17$. Note that the values of surface tension are calculated at the annealing temperature. Additionally, the lattice constants of Ta and Fe [$a_0$(Ta)=0.331 nm and $a_0$(Fe) =0.287 nm] yield a lattice mismatch strain $\varepsilon = 0.15$ for Fe/Ta. Based on the estimated $\varepsilon$ and $\kappa$ and the iron WL observed [Figs. 4(a) and 4(b)], the formation of Fe thin film on Ta is expected to follow the SK growth mode. The same growth mode has been found for Fe nanoparticles on tungsten,[34] which has a surface tension of 2900 ergs/cm$^2$ and a lattice constant of 0.317 nm, close to those of Ta.[31] In our case iron WL was firstly formed before the growth of individual islands ($<1.5$ nm). From 1.5 to 3 nm, the island density increases. Until about 3 nm the island density reaches saturation, and ripening and coalescence occur, and the island density decreases.

In addition to the island size and density, surface tension and interfacial energy can affect the curvature, or the contact angle, of the catalyst island at the catalyst-support interface. The contact angle can be described by Young's equation

$$\cos\theta = (\gamma_{sv} - \gamma_{fs})/\gamma_{fv}, \tag{2}$$

where $\theta$ is the contact angle, $f$, $s$, and $v$ represent film, substrate, and vacuum, respectively, and $\gamma$ is the surface tension. In the case of Fe on Ta, $0 < \cos\theta < 1$ ($\theta = 40° - 90°$) implies that the surface energy of the Ta substrate exceeds that of the Fe/Ta interface. For Fe islands on $SiO_2$, $-1 < \cos\theta < 0$ ($\theta = 130° - 180°$), indicating that the surface energy of $SiO_2$ is less than that of the Fe/$SiO_2$ interface.

By measuring the contact angle, the adhesion energy of the catalyst nanoparticles on the supporting layer can be deduced, which is important for understanding growth modes of CNTs. The adhesion energy $E_{ad}$ can be obtained from the Young-Dupre equation[35]

$$E_{ad} = \gamma_{np}(1 + \cos\theta), \tag{3}$$

where $\gamma_{np}$ is the surface tension of the nanoparticles. In particular, the adhesion energy is obtained at the annealing temperature of 700 °C (same as the growth temperature). The $\gamma_{np}(T)$ can be obtained by[31]

$$\gamma_{np}(T) = \gamma_{np}(T_0) + (T - T_0) \left.\frac{\delta\gamma_{np}}{\delta T}\right|_{T_0}, \tag{4}$$

where $T_0$ is the melting temperature, and for Fe $\gamma_{np}(T_0)$ and $\delta\gamma_{np}/\delta T|_{T_0}$ are 1880 ergs/cm$^2$ and $-0.43$ ergs/cm$^2$ °C, respectively.[31] Similarly, the surface tension of Ta at different temperatures can be calculated. Combining Eqs. (3) and (4), with the obtained contact angles (40°–90 ° for Ta and 130°–180° for $SiO_2$), an adhesion energy of 2239–3954 ergs/cm$^2$ is obtained for Fe/Ta and is 0–800 ergs/cm$^2$ for Fe/$SiO_2$.

The annealing atmosphere may also play a role in restructuring catalyst. Cantoro *et al.* annealed subnanometer Fe thin films under vacuum and different gas atmosphere and found that Fe nanoparticles were formed at very low temperatures (~300 °C) and the average size of the catalyst nanoparticles varied in different gas atmosphere.[21] In our catalytic and plasma CVD growth, annealing was carried out under a hydrogen flow.

### B. CNT growth

There is vast literature on CCVD growth of CNTs on different substrates and multilayer catalysts. Ng *et al.* used a highly efficient combinatorial approach to study the growth of CNTs on various metal underlayers. They found that titanium was the best in terms of low contact resistance and high CNT density.[19,20] Other studies have shown that Al is particularly effective for single walled nanotube (SWNT) growth. It has been found that during annealing the morphology of Al films varied by clustering itself, which enlarges support surface area and segregates small catalyst particles from sintering, thereby enhancing the yield of SWNTs.[21–23] Porous silicon substrates have been shown to facilitate the growth of self-oriented regular CNT arrays, and the enhanced growth was attributed to the large surface areas of porous silicon for carbon molecules permeating and a strong catalyst-substrate adhesion.[36] Studies above have shown the significance of the support on CNT growth. Some of them have demonstrated the dependence of the catalyst particle size or density on the supporting materials. However, there are few studies on the support effect on morphologies of catalyst nanoparticles and the correlation of the support effect with CNT growth. Until recently, environmental TEM (ETEM) has been successfully used to *in situ* observe dynamics of catalyst nanoparticles on $SiO_x$ during CCVD growth of CNTs.[37,38] These studies revealed a complicated CNT growth process, involving interplays between the catalyst nanoparticles and CNTs. However, these studies focused

only on the oxide with low surface tensions. In our study we used cross-sectional TEM to particularly investigate morphologies of Fe nanoparticles on high surface tension Ta and low surface tension $SiO_2$. It was found that catalyst morphologies were distinctly different on two supports. Furthermore, it was discussed as below how the morphologies of catalysts affected CCVD growth of CNTs.

For our CCVD growth of CNTs on Ta and $SiO_2$, the same catalysts and growth conditions were applied. In addition, both supporting layers are stable in the growth environment, which is evidenced by annealing and growing CNTs on both supports alone without Fe. We found that no pinholes and no carbon depositions were formed on the supports (not showing here). In contrast, Al is not stable because its morphology can vary at a given growth temperature.[21–23] The most pronounced difference between the CCVD growths of CNTs on two supports is Fe morphologies, as shown in Figs. 3 and 4. On $SiO_2$ the Fe thin films turn into isolated nanoparticles with large contact angles during annealing, while on Ta iron nanoparticles with small contact angles are formed and anchored on an iron WL.

Distinctly different CNT growth rates on two supports suggest that the catalyst morphology can greatly affect the activity of the catalysts, because in CCVD the rate determining step is the adsorption and decomposition of hydrocarbons by catalyst particles (growth stage I),[8] which depends primarily on the activity of the catalysts. As a comparison, we also conducted CNT growth on $SiO_2$ in PECVD, where the catalyst activity (or catalyst morphology here) is not as critical as in CCVD [the adsorption and decomposition of hydrocarbons are greatly enhanced by the plasma, and the CNT growth rate is only limited by surface diffusion in PECVD (growth stage II)].[8] Our results have shown that a fast growth from $Fe/SiO_2$ can be achieved by PECVD.

The catalyst activity usually degrades during CNT growth due to catalyst poisoning, which occurs when the catalysts are encapsulated by carbon networks (CNT caps or walls) or amorphous carbon. This is well exhibited by our CCVD growth of CNTs on $SiO_2$. As shown in Fig. 1(f), $Fe/SiO_2$ has much larger catalyst surface areas (dense Fe nanoparticles) compared to Fe/Ta [sparse Fe nanoparticles in Fig. 1(c)]. However, the catalyst activity for $Fe/SiO_2$ is significantly reduced. Figure 6(d) also indicates that curved graphite layers cover almost all surface areas of Fe nanoparticles on $SiO_2$ so that the hydrocarbons are limited to access catalysts, thereby greatly reducing CNT growth rate.

Hofmann *et al.* recently have shown that CNT growth is a complicated process involving dynamic interplays between catalyst nanoparticles and carbon networks.[38] They have observed, in atomic scale, tip and base modes of CNT growth from nickel (Ni) nanoparticles on $SiO_x$. They found that Ni nanoparticles reshaped greatly during CNT formation because of a weak support-catalyst interaction and fast self-diffusivity of Ni, and in the end Ni nanoparticles were fully encapsulated by carbon networks and CNT growth was terminated (catalyst poisoning). This growth scenario can be applied to our CCVD growth of CNTs on $Fe/SiO_2$, where the adhesion energy of Fe particles on $SiO_2$ is also low ($0-800$ ergs/cm$^2$) and the self-diffusivity of Fe is close to Ni.[39]

In the case of Fe/Ta, dynamic interplays can still occur between Fe nanoparticles and CNTs, but the magnitude of reshaping greatly decreases because the iron WL pins down Fe nanoparticles with a large adhesion energy of $2239-3954$ ergs/cm$^2$. We speculate that slowing down the catalyst reshaping retards the encapsulation of nanoparticles by carbon networks, so that uncovered areas on nanoparticle surface can still be available to sustain CNT growth (denoted by the strip area on Fe/Ta, as shown in Fig. 8). WL can also be considered as extra catalysts except for the uncovered nanoparticle surface area. As one or few continuous catalyst atomic layers beneath catalyst nanoparticles, WL cannot nucleate growth of CNTs due to its flat morphology, but it may contribute to the adsorption, decomposition, and transportation of carbon atoms to CNT growth edge, as indicated by the arrows in Fig. 8. More experiments should be conducted in the future to elucidate the role of WL in CCVD growth of CNTs. In addition, it would be very interesting to use ETEM to study dynamics of catalysts on high surface tension supports during CCVD growth of CNTs as a comparison to low surface tension oxide supports, since it has been suggested that the cap formation and chiral selectivity of SWNTs may be related dynamically to catalyst particle-carbon network interactions.[38]

The CNT growth mode has been related to dynamic interplays between the catalysts and CNTs and the interactions between the catalyst and support.[38] In our case the adhesion energy $E_d$ was deduced to be $2239-3954$ ergs/cm$^2$ for Fe/Ta as compared to $0-800$ ergs/cm$^2$ for $Fe/SiO_2$, and the tip growth mode was found for CCVD growth of CNTs on $SiO_2$ and the base growth mode on Ta. However, the base growth mode was also observed on $Fe/SiO_2$ using PECVD, although the $E_d$ for $Fe/SiO_2$ is low. In contrast to CCVD, the plasma in PECVD appears to influence the interplays between the catalyst nanoparticles and carbon networks and facilitate the base growth mode.

Lastly, we note that high surface tension materials such as Ta can promote vertically aligned dense CNTs grown on metal supporting layer. This finding is especially compatible with current copper-low $k$ interconnect structure. Although it appears intrinsically difficult to form ultrafine and high density Fe nanoparticles by annealing thin Fe layers on Ta as compared to $SiO_2$, the morphologies of iron nanoparticles combined with the presence of an iron WL have shown to facilitate the sustaining growth of CNTs by CCVD. This observation provides us another perspective/approach on catalyst design for enhanced CNT growth. In contrast, through depositing a very thin layer of metal catalysts on a low surface tension material, such as the deposition of subnanometer thin Fe layer on $SiO_2$, a uniform and dense distribution of fine catalyst nanoparticles can be obtained. This was found to be crucial for the growth of small diameter CNT films with high densities.[9,21,40] However, our study shows that in CCVD catalyst poisoning occurs more easily on $SiO_2$ due to the

morphologies of Fe nanoparticles. To overcome this problem chemical reactivation of catalysts can be used, i.e., using water or oxygen assisted CVD.[9,40]

## V. CONCLUSIONS

In summary, a comparison study has been conducted on the formation of catalyst nanoparticles on metal and oxide supporting layers for CNT growth. Experiments were performed on Fe nanoparticles formed on a high surface tension metal, Ta, and a low surface tension material, $SiO_2$. Distinctly different nanoparticle densities, size distributions, and morphologies were observed after annealing, which can be attributed to different nanoparticle growth modes. The Ta supporting layer promoted the formation of Fe nanoparticles with hemisphere shape and large adhesion energy, leading to fast CNT growth which proceeds according to the base growth mode. In contrast, Fe nanoparticles on $SiO_2$ had a beadlike shape with lower adhesion energy, resulting in a tip growth mode with greatly reduced growth rates. The CNT growth mode was found to be affected by adhesion between the catalyst and substrate as well as CVD process. The enhanced CNT growth rate on Ta was attributed to the morphologies of iron nanoparticles in combination with the presence of an iron WL, which may affect the catalyst-CNT dynamics and catalyst activity.

## ACKNOWLEDGMENTS

The authors would like to acknowledge Dr. Jianlong Li at UT for fruitful discussions and Dr. Xiaoxia Gao in MER at UT for assistance on TEM. They are also grateful for the support from SEMATECH through Advanced Materials Research Center (AMRC), and the fabrication and characterization facilities in Microelectronic Research Center and Center of Nano and Molecular Science and Technology at University of Texas at Austin.

[1]Z. Yao, C. L. Kane, and C. Dekker, Phys. Rev. Lett. **84**, 2941 (2000).
[2]C. Yu, L. Shi, Z. Yao, D. Li, and A. Majumdar, Nano Lett. **5**, 1842 (2005).
[3]M. Yu, O. Lourie, M. J. Dyer, K. Moloni, T. F. Kelly, and R. S. Ruoff, Science **287**, 637 (2000).
[4]M. Fuhrer, H. Park, and P. L. McEuen, IEEE Trans. Nanotechnol. **1**, 78 (2002).
[5]J. Li, Q. Ye, A. Cassell, H. T. Ng, R. Stevens, and J. Han, Appl. Phys. Lett. **82**, 2491 (2003).
[6]J. K. Holt, H. G. Park, Y. Wang, M. Stadermann, A. B. Artyukhin, C. P. Grigoropoulos, A. Noy, and O. Bakajin, Science **312**, 1034 (2006).
[7]Y. J. Jung *et al.*, Nano Lett. **6**, 413 (2006).
[8]S. Hofmann, G. Csanyi, A. C. Ferrari, M. C. Payne, and J. Robertson, Phys. Rev. Lett. **95**, 036101 (2005).
[9]G. Zhang *et al.*, Proc. Natl. Acad. Sci. U.S.A. **102**, 16141 (2005).
[10]H. Cui, O. Zhou, and B. R. Stoner, J. Appl. Phys. **88**, 6072 (2000).
[11]Y. Y. Wang, S. Gupta, R. J. Nemanich, Z. J. Liu, and C. Q. Lu, J. Appl. Phys. **98**, 014312 (2005).
[12]J. Raty, F. Gygi, and G. Calli, Phys. Rev. Lett. **95**, 096103 (2005).
[13]R. T. K. Baker, Carbon **27**, 315 (1989).
[14]C. J. Lee and J. Park, Appl. Phys. Lett. **77**, 3397 (2000).
[15]C. Bower, O. Zhou, W. Zhu, D. J. Werder, and S. Jin, Appl. Phys. Lett. **77**, 830 (2000).
[16]C. Ducati, L. Alexandrou, M. Chhowalla, G. A. J. Amaratunga, and J. Robertson, J. Appl. Phys. **92**, 3299 (2002).
[17]A. M. Cassell, J. A. Raymakers, J. Kong, and H. Dai, J. Phys. Chem. B **103**, 6484 (1999).
[18]D. E. Resasco, W. E. Alvarez, F. Pompeo, L. Balzano, J. E. Herrera, B. Kitiyanan, and A. Borgna, J. Nanopart. Res. **4**, 131 (2002).
[19]H. T. Ng, B. Chen, J. E. Koehne, A. M. Cassell, J. Li, J. Han, and M. Meyyappan, J. Phys. Chem. B **107**, 8484 (2003); A. M. Cassell, Q. Ye, B. A. Cruden, J. Li, P. C. Sarrazin, H. T. Ng, J. Han, and M. Meyyappan, Nanotechnology **15**, 9 (2004).
[20]M. Horibe, M. Nihei, D. Kondo, A. Kawabata, and Y. Awano, Jpn. J. Appl. Phys., Part 1 **44**, 5309 (2005).
[21]M. Cantoro *et al.*, Nano Lett. **6**, 1107 (2006).
[22]L. Delzeit, B. Chen, A. Cassell, R. Stevens, C. Nguyen, and M. Meyyappan, Chem. Phys. Lett. **348**, 368 (2001); L. Delzeit, C. V. Nguyen, B. Chen, R. Stevens, A. Cassell, J. Han, and M. Meyyappan, J. Phys. Chem. B **106**, 5629 (2003).
[23]H. Hongo, F. Nihey, T. Ichihashi, Y. Ochiai, M. Yudasak, and S. Ijima, Chem. Phys. Lett. **380**, 158 (2003).
[24]Y. Y. Wang, B. Li, Z. Yao, L. Shi, and P. S. Ho, Appl. Phys. Lett. **89**, 183113 (2006).
[25]Y. Y. Wang, G. Y. Tang, F. A. M. Koeck, B. Brown, J. M. Garguilo, and R. J. Nemanich, Diamond Relat. Mater. **13**, 1287 (2004).
[26]Y. Y. Wang, S. Gupta, and R. J. Nemanich, Appl. Phys. Lett. **85**, 2061 (2004).
[27]H. Dai, Acc. Chem. Res. **35**, 1035 (2002).
[28]J. A. Floro, E. Chason, and R. D. Twesten, Phys. Rev. Lett. **79**, 3946 (1997).
[29]I. Daruka and A. Barabasi, Phys. Rev. Lett. **79**, 3708 (1997).
[30]M. Ohring, *Materials Science of Thin Films: Deposition and Structure* (Academic, San Diego, 2002), Chap. 7.
[31]K. Tu, J. W. Mayer, and L. C. Feldman, *Electronic Thin Film Science for Electrical Engineers and Materials Scientists* (Macmillan, New York, 1992), Chaps. 2 and 7.
[32]G. A. Somorjai, *Chemistry in Two Dimensions: Surfaces* (Cornell University Press, Ithaca, 1981).
[33]C. Sun and J. C. Berg, J. Chromatogr., A **969**, 59 (2002).
[34]A. Wachowiak, J. Wiebe, M. Bode, O. Pietzsch, M. Morgenstern, and R. Wiesendanger, Science **298**, 577 (2002).
[35]K. S. Gadre and T. L. Alford, J. Appl. Phys. **93**, 919 (2003).
[36]S. Fan, M. G. Chapline, N. R. Franklin, T. W. Tombler, A. M. Cassell, and H. Dai, Science **283**, 512 (1999).
[37]S. Helveg, C. Lopez-Cartes, J. Sehested, P. L. Hansen, B. S. Clausen, J. R. Rostrup-Nielsen, F. Abild-Pedersen, and J. K. Norskov, Nature (London) **427**, 426 (2004).
[38]S. Hofmann *et al.*, Nano Lett. **7**, 602 (2007).
[39]T. Iida, R. Gutheri, and N. Tripathi, Metall. Mater. Trans. B **37B**, 559 (2006).
[40]K. Hata, D. N. Futaba, K. Mizuno, T. Namai, M. Yumura, and S. Lijima, Science **306**, 1362 (2004).